THE JOURNAL OF PHYSICAL CHEMISTRY C

Subscriber access provided by UNIV OF LOUISIANA

C: Physical Processes in Nanomaterials and Nanostructures

# Temperature-Dependent Structural and Spectroscopic Studies of (BiFe)FeO

Andrea Kirsch, M. Mangir Murshed, Melanie J. Kirkham,
Ashfia Huq, Fred Jochen Litterst, and Thorsten M. Gesing

*J. Phys. Chem. C*, **Just Accepted Manuscript** • DOI: 10.1021/acs.jpcc.8b05740 • Publication Date (Web): 08 Nov 2018

**Downloaded from http://pubs.acs.org on November 12, 2018**

**Just Accepted**

"Just Accepted" manuscripts have been peer-reviewed and accepted for publication. They are posted online prior to technical editing, formatting for publication and author proofing. The American Chemical Society provides "Just Accepted" as a service to the research community to expedite the dissemination of scientific material as soon as possible after acceptance. "Just Accepted" manuscripts appear in full in PDF format accompanied by an HTML abstract. "Just Accepted" manuscripts have been fully peer reviewed, but should not be considered the official version of record. They are citable by the Digital Object Identifier (DOI®). "Just Accepted" is an optional service offered to authors. Therefore, the "Just Accepted" Web site may not include all articles that will be published in the journal. After a manuscript is technically edited and formatted, it will be removed from the "Just Accepted" Web site and published as an ASAP article. Note that technical editing may introduce minor changes to the manuscript text and/or graphics which could affect content, and all legal disclaimers and ethical guidelines that apply to the journal pertain. ACS cannot be held responsible for errors or consequences arising from the use of information contained in these "Just Accepted" manuscripts.

ACS Publications

is published by the American Chemical Society. 1155 Sixteenth Street N.W., Washington, DC 20036

Published by American Chemical Society. Copyright © American Chemical Society. However, no copyright claim is made to original U.S. Government works, or works produced by employees of any Commonwealth realm Crown government in the course of their duties.

# Temperature-dependent Structural and Spectroscopic Studies of $(Bi_{1-x}Fe_x)FeO_3$

Andrea Kirsch[a,b], M. Mangir Murshed[a,b*], Melanie J. Kirkham[c], Ashfia Huq[c], F. Jochen Litterst[d], Thorsten M. Gesing[a,b]

[a]University of Bremen, Institute of Inorganic Chemistry and Crystallography, Leobener Straße 7, D-28359, Bremen, Germany

[b]University of Bremen, MAPEX center for materials and processes, Bibliothekstraße 1, D-28359 Bremen, Germany

[c]Chemical and Engineering Materials Division, Oak Ridge National Laboratory, Oak Ridge, Tennessee 37831, USA

[d]Institute for Condensed Matter Physics, Technische Universität Braunschweig, Mendelssohnstr. 3, D-38106 Braunschweig, Germany

*Corresponding author; e-mail address: murshed@uni-bremen.de; phone: +49 (0)421 218 63144; fax: +49 (0)421 218 63144

## Abstract

We report on temperature-dependent structural and spectroscopic features of $(Bi_{1-x}Fe_x)FeO_3$ perovskite for x = 0.15 and 0.25. Samples were synthesized by heating quantum crystalline precursors obtained by polyol method. Crystal structures of each composition were obtained from in-house X-ray, synchrotron X-ray and time-of-flight neutron powder diffraction data Rietveld refinements. Partial replacement of the Bi-site by $Fe^{3+}$ cation significantly changes the crystal-physico-chemical properties such as thermal expansion, polyhedral distortion, Debye temperature, vibrational and magnetic properties. Whereas $BiFeO_3$ is a multiferroic, both $Bi_{0.85}Fe_{0.15}FeO_3$ and $Bi_{0.75}Fe_{0.25}FeO_3$ are found to be superparamagnetic as observed by temperature-dependent Mössbauer and SQUID measurements. Lattice thermal expansion was modeled using the Debye-Einstein-anharmonicity approach. Debye temperatures obtained from mean-squared atomic displacement parameter and lattice thermal expansion are compared. Temperature dependence of selective Raman modes is also analyzed.

## 1. Introduction

Perovskite-type bismuth ferrite $BiFeO_3$ received much attention due to its unique multiferroic properties and promising applications.[1,2] It is concomitantly antiferromagnetic and ferroelectric at room temperature[2] with a Néel temperature of ~ 640 K and Curie temperature of ~1100 K, respectively.[3] The magnetic structure is of G-type and possesses a canted spiral spin arrangement with a propagation direction of <110> (hexagonal setting) with a periodic length of 62 nm.[4] This cycloidal magnetic order does not show net magnetization in the bulk.[5] However, as much as a net magnetization of ~1.5 A $m^2$ $kg^{-1}$ is observed in the nanoparticles when the spiral spin is suppressed.[6] The centrosymmetric distortion of the $Bi^{3+}$ and $Fe^{3+}$ cations along the hexagonal **c**-axis, caused by the stereochemical activity of the $Bi^{3+}$ $6s^2$ lone electron pair[7] (LEP), produces a spontaneous polarization in this direction[8], as shown in Figure 1. The crystal structure is described in the rhombohedral *R*3*c* space group with hexagonal lattice parameters $a$ = 558.76(3) pm and $c$ = 1386.7(1) pm.[9] The $FeO_6$ octahedra are tilted towards each other along the **c**-axis, and the $Bi^{3+}$ cations are located eccentrically in their cavities. The multiferroic properties of $BiFeO_3$ have been widely studied in the form of nanoparticles,[10] single crystals,[11] polycrystals[12] and thin films[13]. Despite intense studies on $BiFeO_3$, some of its physical properties are not fully understood, and debates are ongoing on some contradictory results.[1,6,10] Catalan and Scott (2009) pointed out that further systematic studies on the phase diagram, crystal chemistry, structure and dynamics are of crucial importance for an in-depth exploration.[1] Jia et al. (2014) evidently demonstrated substantial atomic- to nano-scale disordering even in single crystals.[11] They supposed a sluggish phase evolutionary behavior of $BiFeO_3$ that makes it notoriously difficult in producing fully equilibrated single crystals.[11] Indeed, during transformation of an X-ray amorphous powder into a polycrystalline $Bi_2Fe_4O_9$ an intermediate $(Bi_{1-x}Fe_x)FeO_3$ phase was found by $^{57}Fe$ Mössbauer and temperature-dependent X-ray diffraction.[14] In this intermediate structure, the $Bi^{3+}$ site is partially shared by $Fe^{3+}$, which transformed into the $BiFeO_3$ perovskite phase upon increasing temperature.[14] In the present

study, a precursor was synthesized by a sol-gel route using sorbitol as a complexing agent. By subsequent heating, samples with different Fe-content on the Bi position were reproducibly produced. They were characterized by X-ray powder diffraction (XRD), temperature-dependent time-of-flight neutron powder diffraction (NPD), temperature-dependent Raman and $^{57}$Fe Mössbauer spectroscopy. The thermal expansion of the metric parameters as well as the atomic displacement parameters (ADP's) were modelled using a microscopic approach.[15-19]

## 2. Experimental

### 2.1. Synthesis

The stoichiometric $BiFeO_3$ sample was synthesized using the glycerin method[20] and a molar ratio of Bi : Fe = 1 : 1 with an excess of 5% of Bi. 5.25 mmol $Bi(NO_3)_3 \cdot 5H_2O$ (Sigma-Aldrich, ≥ 98%), 5 mmol $Fe(NO_3)_3 \cdot 9H_2O$ (Sigma-Aldrich, ≥ 98%) and 10% glycerin of the total amount of nitrates were heated in a beaker using a glycerin bath to 353 K until $NO_x$ was released and a dried gel was obtained. The mixture was then heated in a furnace at 523 K for 2 h, ground in a mortar, afterwards heated at 773 K for 6 h.

The precursor of the substituted ($(Bi_{1-x}Fe_x)FeO_3$) samples was synthesized by a sol-gel route using sorbitol as a complexing agent. As much as 11 mmol D-Sorbitol was dissolved in 38 mL deionized water under magnetic stirring. Then, stoichiometric amount (7.4 mmol and 6 mmol for x = 0.15 and x = 0.25, respectively) of $Bi(NO_3)_3 \cdot 5H_2O$ (Sigma-Aldrich, ≥ 98%) was added to 10 mmol $Fe(NO_3)_3 \cdot 9H_2O$ (Sigma-Aldrich, ≥ 98%) followed by a few drops of 4 M NaOH (VWR Chemicals, 99.2%) solution to make the mixture slightly basic (pH > 7.0). The mixture was heated in a beaker using a glycerin bath at 353 K until a solid foam was obtained. It was then heated at 523 K for 2 h, ground in a mortar and heated again at 873 K for different periods (10, 20, 30 and 40 min).

### 2.2. Diffraction

***X-ray diffraction***

X-ray powder diffraction data were collected on a X'Pert MPD PRO diffractometer (PANalytical GmbH, Almelo, The Netherlands) equipped with Ni-filtered $CuK_{\alpha 1,2}$ radiation ($\lambda_{K\alpha 1}$ = 154.05929(5) pm, $\lambda_{K\alpha 2}$ = 154.4414(2) pm) and a X'Celerator detector system in Bragg-Brentano geometry. Room-temperature scans were performed from 5 to 85° 2$\theta$ with a step width of 0.0167° 2$\theta$ and a measurement time of 142 s per step. The measurements of samples $(Bi_{0.75}Fe_{0.25})FeO_3$ and $(Bi_{0.85}Fe_{0.15})FeO_3$ were divided into two parts. Dataset-1 was measured between 5° and 85° 2$\theta$ with a step width of 0.0167° 2$\theta$ and a measurement time of 142 s per step, and dataset-2 between 80° and 130° 2$\theta$ with a step width of 0.0167° 2$\theta$ and a measurement time of 284 s per step.

At ambient condition, the X-ray powder diffraction patterns were additionally collected on the high-resolution powder diffractometer at beamline 11-BM at the Advanced Photon Source (APS), Argonne National Laboratory, USA. The wavelength was calibrated to 51.7041(1) pm and the diffraction patterns were recorded from 0.5° to 50° 2$\theta$ with a step width of 0.001° 2$\theta$, and a measurement time of 0.1 s per step. The obtained data were refined using the Rietveld method (DIFFRAC PLUS TOPAS V4.2, Bruker AXS, Karlsruhe, Germany). For profile fitting, the fundamental parameter approach was used. The fundamental parameters for the in-house data were fitted against a $LaB_6$ standard material. The occupancy between $Fe^{3+}$ and $Bi^{3+}$ were refined on the 6*a* position. The ADPs and the occupancy parameters were alternately refined until the satisfactory convergence appeared as suggested by Massa[21].

***Neutron time-of-flight* scattering**

The NPD data were collected on Powgen high-resolution powder diffractometer at the Spallation Neutron Source (SNS), Oak Ridge National Laboratory (ORNL), USA. The temperature-dependent data were measured using the Cryo-furnace Janis between 10 K and 650 K at 10 K steps and a centre wavelength of about 133(1) pm for about half an hour at each temperature. The Rietveld refinements were performed using the GSAS[22] program with EXPGUI interface.[23]

## 2.3. Spectroscopy

### *Raman spectroscopy*

The temperature-dependent Raman spectra were measured on pressed pellets produced from the powder samples. A Horiba LabRam Aramis spectrometer equipped with a 785 nm emission Laser, a slit of 100 μm, a hole of 1000 μm and an exposure time of 10 s with 30 accumulations was used. Data were collected between 100 $cm^{-1}$ and 1000 $cm^{-1}$. For the low-temperature measurements a Linkam cooling stage (THMS600) attached to a pump (LNP95 Cooling Pump) providing a continuous liquid nitrogen flow was used. The high-temperature spectra were collected using a Linkam heating stage (TS1500). Prior to the data collection, the sample was equilibrated for 7 min at the desired temperature. The spectra were fitted with single peaks using the above-mentioned Rietveld software TOPAS V4.2.

### *Mössbauer spectroscopy*

The $^{57}Fe$ Mössbauer absorption spectra were collected using a standard spectrometer with sinusoidal velocity sweep. The 20 mCi $^{57}Co$ in Rhodium γ-radiation source was kept at room temperature. Absorbers of the two powder specimens with thicknesses corresponding to about 15 $mg \cdot cm^{-2}$ of $^{57}Fe$ were included in polyethylene containers. The absorber temperatures were varied using a He-flow cryostat (CRYOVAC®). For data analysis, we used MossWinn 4.0 software.[24]

## 2.4 Magnetic measurements

Temperature-dependent magnetic susceptibility measurements were carried out with a Quantum-Design MPMS-XL-5 SQUID magnetometer equipped with a 5 T magnet in the range from 2 to 300 K at a magnetic field of 0.1 T. The isothermal magnetization was measured at 300 K. The polycrystalline samples were put into a gel bucket covered with a few drops of low viscosity perfluoropolyether based inert oil (Fomblin YL VAC 25/6) and fixed to a nonmagnetic sample holder. Each raw data of magnetic moment was background corrected for the respective diamagnetic contribution of the gel bucket and the inert oil.

# 3. Results and discussion

## 3.1. X-Ray powder diffraction

The in-house X-ray powder diffraction patterns of the samples produced at 873 K using different crystallization times show only reflections of the perovskite-type phase, as given in Figure 2. However, some very weakly intense but sharp reflections can be seen from the synchrotron data (Figure 2). The sources of these reflections were not identified so far, and the frequently occurring impurities in the Bi-Fe-O system such as $Bi_2Fe_4O_9$[25], $Bi_{25}FeO_{40}$[25], $Bi_{24}Fe_2O_{39}$[25], α- $Bi_2O_3$ or β-$Bi_2O_3$[26], or α-$Fe_2O_3$[27] do not belong to these reflections. According to earlier studies[14] Rietveld refinements on this data were performed by concomitantly refining the $Bi^{3+}$ and $Fe^{3+}$ content on the 6*a* (0,0,0) site. It was found that the Fe content on this site decreases with crystallization time, as shown in **Figure 3**. It is reasonable to assume that with increasing crystallization time an exchange occurs between Bi in the precursor-matrix (quantum crystalline/X-ray amorphous) and the Fe on the 6*a* (0,0,0) site, leading to successive decrease of the Fe-content on this site, followed by formation of stoichiometric $BiFeO_3$. The background (broad hump centered at ~31° 2$\theta$ (CuKα)) decreases with increasing crystallization time (Figure 2). As a consequence, the lattice parameter *a* and the micro-strain decrease from 559.4(1) pm to 558.26(3) pm, and from 0.22(2)% to 0.14(1)%, respectively. Opposite, the average crystallite size increases from 13.8(5) to 35.3(7) nm (Figure 3). The samples $(Bi_{0.75}Fe_{0.25})FeO_3$ and $(Bi_{0.85}Fe_{0.15})FeO_3$ of this series were further investigated by other techniques (see below); their refined structural data are given in **Table 1**. Since Bi and Fe share the 6*a* site (0,0,0; *z* fixed), even though their electronic configuration is significantly different ($Z_{Fe}$ = 26; $Z_{Bi}$ = 83), their displacement parameter was refined with constraint (Table 1). Theoretical X-ray patterns (using identical metric parameters) produced by POWDER CELL[28] showed significant difference between, for instance, $BiFeO_3$ and $(Bi_{0.85}Fe_{0.15})FeO_3$, as can be seen from the intensity of the

(*012*) reflection. From a visual inspection, one can draw a comparative agreement between the observed and the simulated patterns, as shown in **Figure 1S** (Supplementary Information). From synchrotron X-ray data Rietveld refinements of $(Bi_{0.85}Fe_{0.15})FeO_3$, of which the plot is shown in **Figure 2S** (Supplementary information), as much as ~5% mullite-type $Bi_2Fe_4O_9$ was identified in the sample. Some $(Bi_{0.85}Fe_{0.15})FeO_3$ reflections show a strong anisotropy, especially the high intense (*110*) reflection. An even more pronounced anisotropic feature can be seen in the (*202*) reflection, as shown in the magnification in the interested region (**Figure 2S**). Consequently, the average crystallite size was estimated to be 45.3(5) nm from the diffraction pattern excluding (*110*), (*202*), (*012*) and (*030*) and almost doubled (75(1) nm) using only the (*110*) reflection. Due to such anisotropies, using separate reflection profiles for the (*110*), (*202*), (*012*) and (*030*) reflections provided better convergence during the structure refinements. Of particular notes, the magnetic spiral spin propagates in the <110> direction, and, consequently the spins rotate in the [110] plane[4].

### 3.2. Neutron powder diffraction

Structural features of the stoichiometric $BiFeO_3$[9] and the ideal perovskite model[9] are given in Table 1. The positional parameters of $(Bi_{0.75}Fe_{0.25})FeO_3$ and $(Bi_{0.85}Fe_{0.15})FeO_3$ together with the isotropic atomic displacement parameters were followed by temperature-dependent NPD, as shown in **Figure 4**. With increasing Fe on the Bi-site (6*a*: 0,0,0: *z* fixed), the Fe(2) (6*a*: 0,0,*z*) gradually shifts away from the hypothetical centroid. That is, Fe(2) shifts about 33 and 38 pm from the centroid for $(Bi_{0.85}Fe_{0.15})FeO_3$ and $(Bi_{0.75}Fe_{0.25})FeO_3$, respectively. This could be explained by an increased distortion of the $BiO_6$ coordination due to smaller ionic radius of $Fe^{3+}$ (64.5 pm) than that of $Bi^{3+}$ (103 pm).[29] Palewicz et al. (2009) studied the evolution of structural parameters of stoichiometric $BiFeO_3$ by neutron powder diffraction below[30] and above[31] room temperature, which increase monotonically with respect to temperature, except a decrease of *y*-coordinate of the O-site.[30] The atomic coordinates change with increasing temperature (Fig. 4).

At about 240 K, a deep minimum has been observed for the change of the *z*-coordinates of the Fe(2)- and O-site in $(Bi_{0.75}Fe_{0.25})FeO_3$. This minimum has been shifted to 260 K for $(Bi_{0.85}Fe_{0.15})FeO_3$. The *x*- and *y*-coordinates of the O-sites of both phases slowly increase up to ~ 450 K followed by a sharp slope (which is at a slightly higher temperature for $(Bi_{0.75}Fe_{0.25})FeO_3$, opposite to the behaviour of the deep minimum temperatures). At this temperature, a sudden frequency drop of the $A_1$-1 mode was observed in the Raman spectra (see later). Moreover, a pronounced change in the slope for the ADP's of the Bi/Fe- and Fe-sites was observed (see later). The changes of bond lengths and bond angles are given in **Figure 5**. The long Bi/Fe-Fe distance (**Figure 5**a) shows a maximum at about ~ 250 K (**Figure 5**a), which could be correlated to the deep minimum observed for the change of the *z*-coordinates of the Fe(2)- and O-sites.

The short Bi/Fe-Fe distance (**Figure 5**b) also shows a point of inflection at 250 K. A maximum in the long Bi-Fe distance was also observed by Palewicz et al. (2007)[31] but only at 550 K. The Fe(2)-O bond length of the fully occupied Fe-position (**Figure 5**e and **5f**) remains nearly unchanged until ~ 400 K for $(Bi_{0.85}Fe_{0.15})FeO_3$ and ~ 450 K for $(Bi_{0.75}Fe_{0.25})FeO_3$. Afterward, the long Fe-O bond length decreases while the short Fe-O bond length increases simultaneously. In general, these bond lengths differ from reported values for $BiFeO_3$ (211.41(17) pm, 194.70(17) pm at 298 K)[30] in a way that the normally huge difference of 16.7(4) pm is decreased to 9(1) pm for $(Bi_{0.85}Fe_{0.15})FeO_3$ (207.87(78) pm, 198.43(67) pm at 300 K) and even more remarkable to 5(2) pm (206(1) pm, 201(09) pm at 300 K) for $(Bi_{0.75}Fe_{0.25})FeO_3$ (**Figure 5**). While the difference in the two bond lengths of the $Fe(2)O_6$ octahedra decreases with a higher Fe-content on the Bi-position, it increases in the $(Bi/Fe)O_6$ octahedra. The long and short Bi/Fe-O distances are determined to be 255.5(7) pm and 220.5(10) pm for $(Bi_{0.75}Fe_{0.25})FeO_3$ and 254.84(79) pm and 222.68(71) for $(Bi_{0.85}Fe_{0.15})FeO_3$ (**Figure 5**), respectively. Compared to calculated values of the model structure of $BiFeO_3$[9] (252.42(171) pm, 231.42(231) pm) the

difference between long and short Bi/Fe-O distance increases from 21(4), 32(1) and 35(2) pm for samples with a Fe-content of 0%, 15% and 25% on the Bi-position, respectively. With increasing temperature, the long Bi/Fe-O bond length linearly increases with a steeper slope from 550 K on. On the contrary, the short Bi/Fe-O distance remains unchanged with a weak rise from ~250 to ~550 K followed by a negative slope afterwards. The Fe-O-Fe angle, as depicted in **Figure 5**, slowly increases for both samples (154.0(6)° to 154.6(7)° for $(Bi_{0.75}Fe_{0.25})FeO_3$; 154.6(4)° to 155.7(5)° for $(Bi_{0.85}Fe_{0.15})FeO_3$) from 10 to 640 K. Palewicz et al. (2007 and 2010) reported an increase of this angle from 154.75(8)[30] to 156.0(1)[31] degree from 5 to 643 K for stoichiometric $BiFeO_3$. The internal O-Fe-O angles slightly decrease with temperature.

The Wang-Liebau eccentricity (WLE) parameter[32] was calculated for the $(Bi/Fe)O_6$ octahedra for the samples as well as for the stoichiometric $BiFeO_3$[31]; their temperature dependency is shown in Figure 3S (Supplementary information). The WLE of the $(Bi/Fe)O_6$ octahedra increases with the Fe content on the Bi-position from $2.34 \cdot 10^{-5}$ over $2.96 \cdot 10^{-5}$ to $3.37 \cdot 10^{-5}$ for a Fe occupancy of 0%, 15% and 25%, respectively. Nevertheless, it is unlikely that the stereochemical activity of lone electron pair (LEP) of the $Bi^{3+}$ cation increases while the Fe content at this site increases. In this case, the octahedral distortion mainly increases due to two different sized ions at a given crystallographic site, as shown in **Figure 6**, where octahedral mean quadratic elongation ($\lambda$)[33] was compared between the $(Bi/Fe)O_6$ and $Fe(2)O_6$ octahedra. As such, a pronounced distortion of the $Bi/FeO_6$ octahedra can be seen for the Bi/Fe sites, and the points of inflection with respect to temperature are comparable to those of interatomic bond distances and angles (**Figure 5**).

The temperature-dependent ADPs of both phases are shown in **Figure 7** along with the fitting model based on the Debye approach suggested by Lonsdale[34], and the fitting parameters are given in **Table 2**. The ADPs at any given temperature follow the order O > Fe > Bi, which

agree well with most of common findings.[30,31] However, the ADPs as well as the static disorder increase with increasing Fe-content in the perovskite. Static disorder calculated from the 0 K intercept of the linear extrapolation of the ADP data down to the Debye temperature agrees well to the values calculated from the direct Debye-fit of the temperature-dependent ADPs which monotonically increases over the whole temperature range. Since the characteristic Debye temperature represents the binding forces between the lattice sites, the consequent change of the atomic Debye temperature ($\theta_{Di}$) upon partial replacement of bismuth by iron is clearly observed (**Table 2**). Whereas the Debye temperatures of Bi/Fe and Fe, for both phases, lie close to each other, the Debye temperature of oxygen atom significantly differs. That is, for instance, the oxygen in $(Bi_{0.75}Fe_{0.25})FeO_3$ locates in a stiffer coordination. Due to this dominant role, of oxygen the mass-weighted Debye temperature of $(Bi_{0.75}Fe_{0.25})FeO_3$ (356 K) is higher than that of $(Bi_{0.85}Fe_{0.15})FeO_3$ (293 K). This result differs from that of $(Bi_{1-x}Re_x)FeO_3$ (Re = La, Eu, Ho) multiferroics, where the Debye temperature is inversely proportional to the compositional x-value.[35]

### 3.2. Spectroscopy

***Raman spectroscopy***

The Brillouin zone-centre optical phonon modes of space group *R*3*c* can be classified as $4A_1 + 5A_2 + 9E$. The $A_1$- and E-modes are polarized along the *z*-axis and the *xy*-plane, respectively, and both are Raman and IR active. Some of the $A_2$ modes calculated at 109, 261, 308, 446, and 579 $cm^{-1}$ are optically silent, however can be observed by inelastic neutron scattering.[36] Raman spectra of the samples are shown in **Figure 8**. Of better resolved intense modes, the peaks at 146.5 $cm^{-1}$ and 174.6 $cm^{-1}$ are observed for $BiFeO_3$, which are assigned to E(TO2) and $A_1$(TO1), respectively.[37] Both of them slightly shift to corresponding higher frequency for $(Bi_{0.85}Fe_{0.15})FeO_3$ (147.3(1) and 174.6(1) $cm^{-1}$) and $(Bi_{0.75}Fe_{0.25})FeO_3$ (148.8(1) and 175.0(1) $cm^{-1}$). First principal studies[37] demonstrated that frequency up to 167 $cm^{-1}$ belongs purely to

Bi-atoms, and Fe-atoms mainly contribute between 152 and 261 $cm^{-1}$, and to higher-wavenumbers. Consequently, the intensity ratio of $I_{147}/I_{175}$ decreases upon successive replacement of Fe in the Bi-site since both the wavenumbers are indicative for one of the sites.[10] The temperature-dependence of E(TO2) and $A_1$(TO1) modes for $BiFeO_3$, $(Bi_{0.75}Fe_{0.25})FeO_3$ and $(Bi_{0.85}Fe_{0.15})FeO_3$ are shown in Figure 4S (Supplementary information). The wavenumber of the modes at 0 K has been obtained from the linear extrapolation of the low-temperature data and listed in Table 3. The mode-Grüneisen parameter was calculated from the volume derivative and listed in Table 1S. The corresponding cell volumes were taken from the respective thermal-expansion model fitting (see later).

***Mössbauer spectroscopy***

The temperature-dependent $^{57}Fe$ Mössbauer spectra are depicted in **Figure 9**. The hyperfine parameters are collected in Table 4. The experimentally determined values of isomer shift (IS) are typical for high spin $Fe^{3+}$ ions.[38] No signals from high spin $Fe^{2+}$ could be resolved; their isomer shifts would lie above about 0.6-0.7 $mm \cdot s^{-1}$.[38,39] Consequently, magnetite ($Fe_3O_4$) as an impurity must be excluded. Comparing the determined hyperfine parameters (Table 3), one can safely assume that any of our samples does not contain impurities such as γ-$Fe_2O_3$[40,41,42] or α-$Fe_2O_3$.[40,43,44] The spectra recorded at 300 K show a superposition of magnetically split patterns (i.e. from sites with static hyperfine fields) and doublet patterns from superparamagnetic sites. Magnetic hyperfine fields in the superparamagnetic fraction are averaged to zero due to fluctuations faster than the nuclear Larmor precession, that is, they must be on the order of GHz. Even at 300 K, one can trace a slowing down of superparamagnetic relaxations for parts of the sample $(Bi_{0.85}Fe_{0.15})FeO_3$, resulting in a broad unresolved background covering about half of the total spectral area. The spectra of both samples at 200 K and 100 K reveal strongly broadened patterns and line shapes that deviate from a Lorentzian profile, which is typical for relaxation effects due to slow superparamagnetic fluctuations (**Fig. 9**). These spectra are shown to demonstrate the general temperature-dependent spectral development. A detailed analysis

would need knowledge of crystallite size distributions and crystallite anisotropy energies correlated with the relaxation time, which lies out of the scope of the present study. We rather concentrate on the analysis of the spectra at 300 and 20 K. The latter can be deconvoluted with static magnetic sextets though the strongly broadened lines of sextet-4 of both samples, indicating that superparamagnetic fluctuations persist even at 20 K. All $Fe^{3+}$ coordination's leading to doublets in the Mössbauer spectra exhibit a high quadrupolar splitting QS of 0.54(1) – 1.08(1) mm/s (**Table 3**). As such, a high distortion of the associated octahedra is expected since the quadrupolar splitting of octahedrally coordinated $Fe^{3+}$ usually increases with a higher distortion.[39] Interestingly, these high QS are strongly reduced (-0.02 mm/s – 0.04 mm/s) when the samples are cooled down to 20 K, and static magnetic sextets of these sites have evolved. The apparent vanishing of QS can be related to a wide distribution of angles between magnetic hyperfine field and electric field gradient due to disorder. The IS of the doublets are smaller than those of the sextets, leading to higher charge density at the nucleus, thus smaller bond length. The sum of the already static magnetic sextets (1+2, **Table 3**) in the room-temperature spectra represent a relative area of 36(4)% and 31(4)% for $(Bi_{0.75}Fe_{0.25})FeO_3$ and $(Bi_{0.85}Fe_{0.15})FeO_3$ of the spectra, respectively. However, the relative population of the magnitudes of sextet-1 and sextet-2 is different in the samples at any given temperature (Table 3). The relative areas of the doublets add up to 65(4)% in $(Bi_{0.75}Fe_{0.25})FeO_3$ and turn to sextet-3 and sextet-4 in the 20 K spectrum. Whereas, in the room-temperature spectrum of $(Bi_{0.85}Fe_{0.15})FeO_3$ two doublets add up with a singlet to 69(6)%. Interestingly, sextet-3 and sextet-4 in the 20 K spectrum add up to only 55(4)% of the relative area. This corresponds to the area of the singlet in the room-temperature spectrum. As compared to the obtained hyperfine parameters of a $BiFeO_3$ sample with 14 nm sized crystals of Park et al. (2007), the determined parameters are comparable to those of $(Bi_{0.75}Fe_{0.25})FeO_3$.[6] In general, the Mössbauer lines are quite broadened showing values from 0.30(1) to 0.88(1) mm/s (**Table 3**), suggesting some sorts of disorder around the Fe-sites. Blaauw and van der Woude[45] pointed out that even in

stoichiometric $BiFeO_3$ all Fe-sites are not completely equivalent and the crystallographic structure is of more complicated character.

### 3.4. DEA Modelling

Despite a large number of papers published on $BiFeO_3$, a complete set of elastic moduli were not experimentally obtained. As such, discrepancies between the experimentally obtained bulk modulus could not be judged, as given in Table 2S (Supplementary information). Herein, we consider the ab initio based six independent elastic moduli ($C_{ij}$) of the rhombohedral symmetry and the corresponding bulk modulus for thermal expansion modeling. The change of the metric parameters with temperature obtained from neutron powder diffraction measurements are shown in **Figure 10**. The lattice thermal expansion was modelled using the DEA approach[15,17,18] and the fitting parameters are listed in **Table 4**. For comparison, we also analysed the temperature-dependent neutron powder data of $BiFeO_3$.[3,29,30] For each case, the simulation of the metric parameters shows an excellent fit considering only a single Debye term for the calculation of temperature-dependent vibrational energy. The integral term of the Debye function was numerically evaluated leading to Debye temperatures of 357(89), 392(81) and 375(5) K for $(Bi_{0.75}Fe_{0.25})FeO_3$, $(Bi_{0.85}Fe_{0.15})FeO_3$ and $BiFeO_3$, respectively (Table 4). Notably, the neutron data of $BiFeO_3$ were limited only to 300 K. Kallaev et al. reported a Debye temperature of 500 K[35] calculated from the heat capacity ($C_V$). It is quite surprising that the Debye temperature evaluated from $C_V$ measurements is higher than those of thermal expansion calculations. However, the authors took the bulk modulus of $Pb(Ti,Zr)O_3$; therefore, the reliability of such physical parameter is difficult to compare. The thermoelastic fitting parameter leads to thermodynamic Grüneisen parameter of $BiFeO_3$ to be $\gamma = 0.87$. Since the thermoelastic parameter ($k_D$) does not significantly change upon substitution of Bi with Fe (Table 4), a reasonable assumption of the Grüneisen parameter of 0.87 would lead to bulk moduli of 91(1) and 98(1) GPa for $(Bi_{0.85}Fe_{0.15})FeO_3$ and $(Bi_{0.75}Fe_{0.25})FeO_3$, respectively. The

axial thermal expansion coefficient follows as $\alpha_c > \alpha_a$ (with $\alpha_a$ and $\alpha_c$ for *a*- and *c*-cell parameters). It shows an anomaly with a minimum at about 400 K for $(Bi_{0.75}Fe_{0.25})FeO_3$ and 420 K for $(Bi_{0.85}Fe_{0.15})FeO_3$, as seen in the insets of **Figure 10**. However, these anomalies have not been seen for stoichiometric $BiFeO_3$[31] as within the temperature range (10 K -300 K) the magnetic phase does not change (AFM for the whole range). Whether the TEC anomalies observed for both $(Bi_{0.75}Fe_{0.25})FeO_3$ and $(Bi_{0.85}Fe_{0.15})FeO_3$ are associated with magneto-volume effect due to corresponding magnetic phase transition is not clear at this stage.

### 3.5. SQUID analysis

To further evaluate the magnetic properties of the samples, SQUID measurements on the samples $(Bi_{0.85}Fe_{0.15})FeO_3$, $(Bi_{0.75}Fe_{0.25})FeO_3$ and stoichiometric $BiFeO_3$ were performed. The magnetic hysteresis curves, as shown in **Figure 11**, clearly reveal a superparamagnetic behavior for $(Bi_{0.85}Fe_{0.15})FeO_3$ and $(Bi_{0.75}Fe_{0.25})FeO_3$ as already seen in the Mössbauer spectra (Figure 9). An enlarged view of these curves clearly shows no hints of remanence. The values obtained for the magnetization of $BiFeO_3$ however well fit those earlier reported.[6,10,46,47] The magnetization of $(Bi_{0.85}Fe_{0.15})FeO_3$ and $(Bi_{0.75}Fe_{0.25})FeO_3$ on the contrary is found to be very high with a magnetic saturation ($M_s$) of 7.3 A $m^2$ $kg^{-1}$ and 7.8 A $m^2$ $kg^{-1}$ at 300 K and 5 T, respectively. In comparison, some reported values for $BiFeO_3$ are 0.2 A $m^2$ $kg^{-1}$,[48] ~0.35 A $m^2$ $kg^{-1}$ [49],1.4 A $m^2$ $kg^{-1}$ [50], 1.55 A $m^2$ $kg^{-1}$ [6] and 3.4 A $m^2$ $kg^{-1}$ [51]. Mazumder et al. (2007)[47] observed saturation of as high as ~7 A $m^2$ $kg^{-1}$ for nano-sized $BiFeO_3$, which is comparable to the present study. Recently, Guria et al. (2014)[52] found superparamagnetic behaviour of paramagnetic $Sm_2O_3$ at room temperature. This finding is unusual as superparamagnetism is generally known to be associated with ferromagnetic or ferrimagnetic materials due to size effects. They synthesized variously shaped nanostructures and stated that these differences in the magnetism clearly can be lead back to the difference in the growth patterns of the materials.[52] Our materials also show a strong anisotropy in the (202) and (110)

planes, where the latter one is the rotation plane of the magnetic moments that develop the spiral magnetic structure.[4] Whether the modified magnetism is due to strong anisotropy or due to disappearing of the spiral spin ordering with higher spin concentration at the Bi-position requires further investigations.

## 4. Conclusion

From the neutron powder diffraction, the most intense antiferromagnetic Bragg reflections at a *d*-value of about 455(2) pm was observed between 10 and 650 K. On the other hand, both the SQUID data and the Mössbauer analyses confirmed that $(Bi_{0.85}Fe_{0.15})FeO_3$ and $(Bi_{0.75}Fe_{0.25})FeO_3$ show superparamagnetic behaviours between 2 K and 300 K. But the concomitant occurrence of antiferromagnetism and superparamagnetism between 10 K and 300 K deserves at least an *ad hoc* explanation. For samples with an average crystallite sizes less than 62 nm, the helimagnetic ordering is not expected, leading to vanish the AFM ordering at any given temperatures. In this respect, the crystallite size-dependent magnetization can be comparable with that of nanoparticle $BiFeO_3$.[6] If the distribution of the crystallite sizes consists of a reasonable portion with sizes ≥ 62 nm, the magnetic reflections can be explained. And, with increasing temperature, the average crystallite size increases due to Oswald ripening, leading to a narrow distribution of crystallites (≥ 62 nm). Consequently, the magnetostriction may develop at higher temperatures, as can be seen from the thermal expansion above 400 K. Moreover, since ferroelectricity and magnetism in these materials are driven by the Bi and Fe sites, respectively, any ferroelectric into paraelectric phase transition can involve significant changes of the Bi/Fe dynamics, leading to axial strong anharmonicity. The consequent compensation may develop volumetric thermal expansion minima, as seen above 400 K.

## Supporting Information

Simulated and measured X-ray powder patterns of $BiFeO_3$ and $(Bi_{1-x}Fe_x)FeO_3$. Rietveld patterns of $(Bi_{0.85}Fe_{0.15})FeO_3$ for the synchrotron X-ray data (APS). Temperature-dependent Wang-Liebau eccentricity parameter of the $(Bi/Fe)O_6$ octahedra. Temperature-dependent Raman modes and their Grüneisen parameters. Elastic coefficients and bulk moduli of $BiFeO_3$.

*Acknowledgement*

We gratefully acknowledge the magnetic measurements of Dr. Serhiy Demeshko and Prof. Dr. Franc Meyer (University of Göttingen). NPD was conducted at ORNL's Spallation Neutron Source sponsored by the Scientific User Facilities Division, Office of Basic Energy Sciences, US Department of Energy. We thank University of Bremen for the financial support for A.K and MMM.

## Reference

(1) Catalan, G.; Scott, J. F. Physics and Applications of Bismuth Ferrite. *Adv. Mater.* **2009**, *21* (24), 2463–2485.

(2) Park, J.-G.; Le, M. D.; Jeong, J.; Lee, S. Structure and Spin Dynamics of Multiferroic $BiFeO_3$. *J. Phys. Condens. Matter* **2014**, *26* (43), 433202.

(3) Fischer, P.; Polomska, M.; Sosnowska, I.; Szymanski, M. Temperature Dependence of the Crystal and Magnetic Structures of $BiFeO_3$. *J. Phys. C Solid State Phys.* **1980**, *13* (10), 1931–1940.

(4) Sosnowska, I.; Neumaier, T. P.; Steichele, E. Spiral Magnetic Ordering in Bismuth Ferrite. *J. Phys. C Solid State Phys.* **1982**, *15*, 4835–4846.

(5) Ederer, C.; Spaldin, N. A. Influence of Strain and Oxygen Vacancies on the Magnetoelectric Properties of Multiferroic Bismuth Ferrite. *Phys. Rev. B* **2005**, *71* (22), 224103.

(6) Park, T.; Papaefthymiou, G. C.; Viescas, A. J.; Moodenbaugh, A. R.; Wong, S. S. Size-Dependent Magnetic Properties of Single-Crystalline Multiferroic $BiFeO_3$ Nanoparticles. *Nano Lett.* **2007**, *7* (3), 766–772.

(7) Ravindran, P.; Vidya, R.; Kjekshus, A.; Fjellvåg, H.; Eriksson, O. Theoretical Investigation of Magnetoelectric Behavior in $BiFeO_3$. *Phys. Rev. B* **2006**, *74* (22), 224412.

(8) Ruette, B.; Zvyagin, S.; Pyatakov, A. P.; Bush, A.; Li, J. F.; Belotelov, V. I.; Zvezdin, A. K.; Viehland, D. Magnetic-Field-Induced Phase Transition in $BiFeO_3$ Observed by High-Field Electron Spin Resonance: Cycloidal to Homogeneous Spin Order. *Phys. Rev. B* **2004**, *69* (6), 64114.

(9) Moreau, J. M.; Michel, C.; Gerson, R.; James, W. J. Ferroelectric $BiFeO_3$ X-Ray and Neutron Diffraction Study. *J. Phys. Chem. Solids* **1971**, *32*, 1315–1320.

(10) Huang, F.; Wang, Z.; Lu, X.; Zhang, J.; Min, K.; Lin, W.; Ti, R.; Xu, T.; He, J.; Yue, C.; et al. Peculiar Magnetism of $BiFeO_3$ Nanoparticles with Size Approaching the Period of the Spiral Spin Structure. *Sci. Rep.* **2013**, *3* (1), 2907.

(11) Jia, C.-L.; Jin, L.; Wang, D.; Mi, S.-B.; Alexe, M.; Hesse, D.; Reichlova, H.; Marti, X.; Bellaiche, L.; Urban, K. W. Nanodomains and Nanometer-Scale Disorder in Multiferroic Bismuth Ferrite Single Crystals. *Acta Mater.* **2015**, *82*, 356–368.

(12) Kalinin, S. V; Suchomel, M. R.; Davies, P. K.; Bonnell, D. A. Potential and Impedance Imaging of Polycrystalline $BiFeO_3$ Ceramics. *J. Am. Ceram. Soc.* **2002**, *85* (12), 3011–

3017.
(13) Wang, J.; Neaton, J. B.; Zheng, H.; Nagarajan, V.; Ogale, S. B.; Liu, B.; Viehland, D.; Schlom, D. G.; Waghmare, U. V.; Spaldin, N. A.; et al. Epitaxial $BiFeO_3$ Multiferroic Thin Film Heterostructures. *Science (80-. ).* **2003**, *299*, 1719–1722.
(14) Kirsch, A.; Murshed, M. M.; Gaczynski, P.; Becker, K.-D.; Gesing, T. M. $Bi_2Fe_4O_9$: Structural Changes from Nano- to Micro-Crystalline State. *Zeitschrift für Naturforsch. B J. Chem. Sci.* **2016**, *71* (5), 447–455.
(15) Murshed, M. M.; Zhao, P.; Fischer, M.; Huq, A.; Alekseev, E. V.; Gesing, T. M. Thermal Expansion Modeling of Framework-Type $Na[AsW_2O_9]$ and $K[AsW_2O_9]$. *Mater. Res. Bull.* **2016**, *84*, 273–282.
(16) Murshed, M. M.; Mendive, C. B.; Curti, M.; Šehović, M.; Friedrich, A.; Fischer, M.; Gesing, T. M. Thermal Expansion of Mullite-Type $Bi_2Al_4O_9$: A Study by X-Ray Diffraction, Vibrational Spectroscopy and Density Functional Theory. *J. Solid State Chem.* **2015**, *229*, 87–96.
(17) Murshed, M. M.; Mendive, C. B.; Curti, M.; Nénert, G.; Kalita, P. E.; Lipinska, K.; Cornelius, A. L.; Huq, A.; Gesing, T. M. Anisotropic Lattice Thermal Expansion of PbFeBO4 : A Study by X-Ray and Neutron Diffraction, Raman Spectroscopy and DFT Calculations. *Mater. Res. Bull.* **2014**, *59*, 170–178.
(18) Murshed, M. M.; Šehović, M.; Fischer, M.; Senyshyn, A.; Schneider, H.; Gesing, T. M. Thermal Behavior of Mullite between 4 K and 1320 K. *J. Am. Ceram. Soc.* **2017**, *100* (11), 5259–5273.
(19) Murshed, M. M.; Gesing, T. M. Anisotropic Thermal Expansion and Anharmonic Phonon Behavior of Mullite-Type $Bi_2Ga_4O_9$. *Mater. Res. Bull.* **2013**, *48* (9), 3284–3291.
(20) Gesing, T. M.; Fischer, R. X.; Burianek, M.; Mühlberg, M.; Debnath, T.; Rüscher, C. H.; Ottinger, J.; Buhl, J.-C.; Schneider, H. Synthesis and Properties of Mullite-Type $(Bi_{1-x}Sr_x)_2(M1_{1-y}M2_y)_4O_{9-x}$ (M=Al, Ga, Fe). *J. Eur. Ceram. Soc.* **2011**, *31* (16), 3055–3062.
(21) Massa, W. *Kristallstrukturbestimmung*, 7. Auflage.; Springer Verlag, 2011.
(22) Larson, A. C.; Von Dreele, R. B. General Structure Analysis System (GSAS), 2004, 86–748.
(23) Toby, B. H. EXPGUI , a Graphical User Interface for GSAS. *Journal of Applied Crystallography*, 2001, *34*, 210–213.
(24) Klencsár, Z. MossWinn 4.0 Manual.
(25) Liu, T.; Xu, Y.; Zhao, J. Low-Temperature Synthesis of $BiFeO_3$ via PVA Sol-Gel Route. *J. Am. Ceram. Soc.* **2010**, *93* (11), 3637–3641.
(26) Chen, J.-C.; Wu, J.-M. Dielectric Properties and Ac Conductivities of Dense Single-Phased $BiFeO_3$ Ceramics. *Appl. Phys. Lett.* **2007**, *91* (18), 182903.
(27) Da Silva, K. L.; Menzel, D.; Feldhoff, A.; Kübel, C.; Bruns, M.; Paesano, A.; Düvel, A.; Wilkening, M.; Ghafari, M.; Hahn, H.; et al. Mechanosynthesized $BiFeO_3$ Nanoparticles with Highly Reactive Surface and Enhanced Magnetization. *J. Phys. Chem. C* **2011**, *115* (15), 7209–7217.
(28) Kraus, W.; Nolze, G. POWDER CELL – a Program for the Representation and Manipulation of Crystal Structure and Calculation of the Resulting X-Ray Powder Patterns. *J. Appl. Crystallogr.* **1996**, *29* (3), 301–303.
(29) Shannon, R. D. Revised Effective Ionic Radii and Systematic Studies of Interatomie Distances in Halides and Chalcogenides. *Acta Crystallogr.* **1976**, *A32*, 751–767.
(30) Palewicz, a; Sosnowska, I.; Przeniosło, R.; Hewat, a W. $BiFeO_3$ Crystal Structure at Low Temperatures. *Acta Phys. Pol. A* **2010**, *117* (2), 296–301.
(31) Palewicz, A.; Przeniosło, R.; Sosnowska, I.; Hewat, A. W. Atomic Displacements in $BiFeO_3$ as a Function of Temperature: Neutron Diffraction Study. *Acta Crystallogr. Sect. B Struct. Sci.* **2007**, *63* (4), 537–544.

(32) Wang, X.; Liebau, F. Influence of Polyhedron Distortions on Calculated Bond-Valence Sums for Cations with One Lone Electron Pair. *Acta Crystallogr. Sect. B Struct. Sci.* **2007**, *63* (2), 216–228.
(33) Robinson, K.; Gibbs, G. V.; Ribbe, P. H. Quadratic Elongation: A Quantitative Measure of Distortion in Coordination Polyhedra. *Science (80-. ).* **1971**, *172*, 567–570.
(34) Lonsdale, K. Vibration Amplitudes of Atoms in Cubic Crystals. *Acta Crystallogr.* **1948**, *1* (3), 142–149.
(35) Kallaev, S. N.; Mitarov, R. G.; Omarov, Z. M.; Gadzhiev, G. G.; Reznichenko, L. A. Heat Capacity of $BiFeO_3$-Based Multiferroics. *J. Exp. Theor. Phys.* **2014**, *118* (2), 279–283.
(36) Delaire, O.; Stone, M. B.; Ma, J.; Huq, A.; Gout, D.; Brown, C.; Wang, K. F.; Ren, Z. F. Anharmonic Phonons and Magnons in $BiFeO_3$. *Phys. Rev. B* **2012**, *85* (6), 64405.
(37) Hermet, P.; Goffinet, M.; Kreisel, J.; Ghosez, P. Raman and Infrared Spectra of Multiferroic Bismuth Ferrite from First Principles. *Phys. Rev. B* **2007**, *75* (22), 220102.
(38) Murad, E. Mössbauer Spectroscopy of Clays, Soils and Their Mineral Constituents. *Clay Miner.* **2010**, *45* (4), 413–430.
(39) Burns, R. G. Mineral Mössbauer Spectroscopy : Correlations between Chemical Shift and Quadrupole Splitting Parameters. *Hyperfine Interact.* **1994**, *91*, 739–745.
(40) Zhang, X.; Niu, Y.; Meng, X.; Li, Y.; Zhao, J. Structural Evolution and Characteristics of the Phase Transformations between α-$Fe_2O_3$, $Fe_3O_4$ and γ-$Fe_2O_3$ Nanoparticles under Reducing and Oxidizing Atmospheres. *CrystEngComm* **2013**, *15* (40), 8166–8172.
(41) Zakharova, I. N.; Shipilin, M. A.; Alekseev, V. P.; Shipilin, A. M. Mössbauer Study of Maghemite Nanoparticles. *Tech. Phys. Lett.* **2012**, *38* (1), 55–58.
(42) Ramos Guivar, J. A.; Bustamante, A.; Flores, J.; Mejía Santillan, M.; Osorio, A. M.; Martínez, A. I.; De Los Santos Valladares, L.; Barnes, C. H. W. Mössbauer Study of Intermediate Superparamagnetic Relaxation of Maghemite (γ-$Fe_2O_3$) Nanoparticles. *Hyperfine Interact.* **2014**, *224* (1–3), 89–97.
(43) Ayyub, P.; Multani, M.; Barma, M.; Palkar, V. R.; Vijayaraghavan, R. Size-Induced Structural Phase Transitions and Hyperfine Properties of Microcrystalline $Fe_2O_3$. *J. Phys. C Solid State Phys.* **1988**, *21* (11), 2229–2245.
(44) Kistner, O. C.; Sunyar, A. W. Evidence for Quadrupole Interaction of Fe57m, and Influence of Chemical Binding on Nuclear Gamma-Ray Energy. *Phys. Rev. Lett.* **1960**, *4*, 412–415.
(45) Blaauw, C.; van der Woude, F. Magnetic and Structural Properties of $BiFeO_3$. *J. Phys. C Solid State Phys.* **1973**, *6*, 1422–1431.
(46) Vijayanand, S.; Mahajan, M. B.; Potdar, H. S.; Joy, P. A. Magnetic Characteristics of Nanocrystalline Multiferroic $BiFeO_3$ at Low Temperatures. *Phys. Rev. B* **2009**, *80* (6), 64423.
(47) Mazumder, R.; Devi, P. S.; Bhattacharya, D.; Choudhury, P.; Sen, A.; Raja, M. Ferromagnetism in Nanoscale BiFeO3. *Appl. Phys. Lett.* **2007**, *91*, 62510-1–3.
(48) Mocherla, P. S. V; Karthik, C.; Ubic, R.; Ramachandra Rao, M. S.; Sudakar, C. Effect of Microstrain on the Magnetic Properties of $BiFeO_3$ Nanoparticles. *Appl. Phys. Lett.* **2014**, *105* (13), 132409.
(49) Wang, X.; Zhang, Y.; Wu, Z. Magnetic and Optical Properties of Multiferroic Bismuth Ferrite Nanoparticles by Tartaric Acid-Assisted Sol–gel Strategy. *Mater. Lett.* **2010**, *64* (3), 486–488.
(50) Lopes, A. M. L.; Araújo, J. P.; Ferdov, S. Room Temperature Synthesis of $Bi_{25}FeO_{39}$ and Hydrothermal Kinetic Relations between Sillenite- and Distorted Perovskite-Type Bismuth Ferrites. *Dalt. Trans.* **2014**, *43* (48), 18010–18016.
(51) Ortiz-Quiñonez, J. L.; Díaz, D.; Zumeta-Dubé, I.; Arriola-Santamaría, H.; Betancourt, I.; Santiago-Jacinto, P.; Nava-Etzana, N. Easy Synthesis of High-Purity $BiFeO_3$

Nanoparticles: New Insights Derived from the Structural, Optical, and Magnetic Characterization. *Inorg. Chem.* **2013**, *52* (18), 10306–10317.

(52) Guria, A. K.; Dey, K.; Sarkar, S.; Patra, B. K.; Giri, S.; Pradhan, N. Tuning the Growth Pattern in 2D Confinement Regime of $Sm_2O_3$ and the Emerging Room Temperature Unusual Superparamagnetism. *Sci. Rep.* **2014**, *4* (1), 6514.

## Table and Figure captions

**Table 1.** Crystal structural parameters of $BiFeO_3$[9], $(Bi_{0.75}Fe_{0.25})FeO_3$ and $(Bi_{0.85}Fe_{0.15})FeO_3$.

**Table 2.** Fitting parameters of the mean-squared isotropic displacement parameters (ADPs).

**Table 3.** Hyperfine parameters of $(Bi_{1-x}Fe_x)FeO_3$. The standard deviations given in the parentheses.

**Table 4**. Fitting parameters of the modelled temperature-dependent metric parameters.

**Figure 2.** X-ray diffraction patterns of $(Bi_{1-x}Fe_x)FeO_3$ samples produced at 873 K for 0, 10, 20, 30 and 40 min, measured in-house (left panel) and at APS, Argonne, USA (right panel) facilities. Unindexed reflections appeared in the synchrotron X-ray patterns are marked by arrows.

**Figure 3.** Structural parameters derived from the in-house X-ray data Rietveld refinements on the samples produced at 873 K for 0, 10, 20, 30 and 40 min, respectively.

**Figure 4.** Temperature-dependent changes of selective atomic coordinates obtained from neutron time-of-flight powder diffraction data Rietveld refinements.

**Figure 5.** Coordination and connectivity in $(Bi_{1-x}Fe_x)FeO_3$ (top) and the changes of selective structural parameters with temperature (bottom).

**Figure 6.** Temperature-dependent octahedral mean quadratic elongation ($\lambda$) of the $(Bi/Fe)O_6$ and $Fe(2)O_6$ octahedra of $(Bi_{1-x}Fe_x)FeO_3$.

**Figure 7.** Temperature-dependent isotropic mean-squared atomic displacement parameters (ADPs) of the atoms along with the respective Debye model fit. The circle, square and diamond refer to $BiFeO_3$, $(Bi_{0.85}Fe_{0.15})FeO_3$ and $(Bi_{0.75}Fe_{0.25})FeO_3$, respectively.

**Figure 8.** left panel: Low-temperature (78 K) Raman spectra along with the compound as well as component fit models. Right panel: Temperature-dependent Raman spectra of $(Bi_{0.75}Fe_{0.15})FeO_3$; temperature increases from 78 K (bottom) to 610 K (top) at 10 K step and from 350 K on at 20 K step.

**Figure 9.** Temperature-dependent $^{57}Fe$ Mössbauer absorption spectra of $(Bi_{0.75}Fe_{0.25})FeO_3$ (a) and $(Bi_{0.85}Fe_{0.15})FeO_3$ (b).

**Figure 10**. Temperature-dependent metric parameters and respective thermal expansion coefficient (TEC, inset) of $(Bi_{0.75}Fe_{0.25})FeO_3$ (left panel) and $(Bi_{0.85}Fe_{0.15})FeO_3$ (right panel).

**Figure 11**. Left panel: Temperature-dependent Fc (0.1 T; cooling and heating) magnetization of $(Bi_{0.85}Fe_{0.15})FeO_3$, $(Bi_{0.75}Fe_{0.25})FeO_3$ and $BiFeO_3$. Right panel: Magnetic hysteresis curves of $(Bi_{0.85}Fe_{0.15})FeO_3$, $(Bi_{0.75}Fe_{0.25})FeO_3$ and $BiFeO_3$ with magnification (inset).

# Tables and figures

## Table 1

| | | | | | | |
|---|---|---|---|---|---|---|
| **Ideal model**[9] | | | | | | |
| Atom | Wyckoff position | *x* | *y* | *z* | Occupancy | *B* /pm$^3$ x10$^4$ |
| Bi | 6*a* | 0 | 0 | 0 | 1 | |
| Fe | 6*a* | 0 | 0 | 0.25 | 1 | |
| O | 18*b* | 0.5 | 0 | 0 | 1 | |
| **BiFeO3**[9] | | | | | | |
| *a* = 558.76(3) pm, *c* = 1386.7(1) pm | | | | | | |
| Bi | 6*a* | 0 | 0 | 0 | 1 | 0.5 |
| Fe | 6*a* | 0 | 0 | 0.2212(15) | 1 | 0.8 |
| O | 18*b* | 0.443(2) | 0.012(4) | 0.9543(20) | 1 | - |
| **$(Bi_{0.85}Fe_{0.15})FeO_3$*** | | | | | | |
| *a* = 558.19(4) pm, *b* = 1385.4(2) pm, *R*wp =0.024, *R*p = 0.083, GOF = 1.64 | | | | | | |
| Bi/Fe | 6*a* | 0 | 0 | 0 | 0.85(1)/0.15(1) | 0.143(6)<br>*1.3(2)* |
| Fe(2) | 6*a* | 0 | 0 | 0.22049(7)<br>*0.2196(4)* | 1 | 0.13(2)<br>*0.32(7)* |
| O | 18*b* | 0.4602(9)<br>*0.453(1)* | 0.0348(7)<br>*0.027(1)* | 0.9470(3)<br>*0.9507(6)* | 1 | 0.8(1)<br>*1.11(8)* |
| **$(Bi_{0.75}Fe_{0.25})FeO_3$*** | | | | | | |
| *a* = 557.53(5), *b* = 1383.2(3), *R*wp =0.037, *R*p = 0.082, GOF = 3.96 | | | | | | |
| Bi/Fe | 6*a* | 0 | 0 | 0 | 0.75(1)/0.25(1) | 0.183(9)<br>*1.7(2)* |
| Fe(2) | 6*a* | 0 | 0 | 0.2194(1)<br>*0.2193(5)* | 1 | 0.183(9)<br>*0.63(8)* |
| O | 18*b* | 0.459(1)<br>*0.456(2)* | 0.0390(9)<br>*0.033(2)* | 0.9421(4)<br>***0.9504(7)*** | 1 | 0.4(1)<br>*1.6(2)* |

*values in normal and italic are obtained by synchrotron X-ray and neutron time-of-flight powder data Rietveld refinement, respectively.

## Table 2

| | $Bi_{0.85}Fe_{0.15}FeO_3$ | | $Bi_{0.75}Fe_{0.25}FeO_3$ | |
|---|---|---|---|---|
| Atom | $\theta_{Di}$ /K | $B_{sta}$ /pm$^2$ | $\theta_{Di}$ /K | $B_{sta}$ /pm$^2$ |
| Bi/Fe | 161(3) | 71(7) | 184(5) | 139(1) |
| Fe | 426(10) | 4.5(1) | 455(9) | 40(2) |
| O | 647(11) | 63(7) | 854(23) | 160(6) |

| | | | | |
|---|---|---|---|---|
| **Mass weighted** | **293(10)** | **-** | **356(13)** | **-** |

$B_{sta}$ refers to static disorder of the respective atom. The estimated uncertainty is given in the parentheses.

**Table 3**

| Fit | *IS /mm s$^{-1}$ | QS /mm s$^{-1}$ | Bhf /T | Γ /mm s$^{-1}$ | Rel. area /% |
|---|---|---|---|---|---|
| | | **$(Bi_{0.75}Fe_{0.25})FeO_3$** | | | |
| *Sextets* | | **300 K** | | | |
| 1 | 0.36(1) | 0.16(1) | 49.4(1) | 0.40(1) | 20(2) |
| 2 | 0.35(1) | 0.02(1) | 48.0(1) | 0.50(1) | 16(2) |
| *Doublets* | | | | | |
| 3 | 0.29(1) | 0.54(1) | | 0.40(1) | 37(2) |
| 4 | 0.27(1) | 1.00(1) | | 0.40(1) | 28(2) |
| *Sextets* | | **20 K** | | | |
| 1 | 0.48(1) | 0.16(1) | 54.9(1) | 0.36(1) | 18(2) |
| 2 | 0.47(1) | 0.08(1) | 53.2(1) | 0.40(1) | 17(2) |
| 3 | 0.42(1) | 0.02(1) | 50.3(1) | 0.54(1) | 37(2) |
| 4 | 0.40(1) | -0.02(1) | 47.0(1) | 0.84(1) | 28(2) |
| | | **$(Bi_{0.85}Fe_{0.15})FeO_3$** | | | |
| *Sextets* | | **300 K** | | | |
| 1 | 0.35 | 0.16(1) | 49.4(1) | 0.40(1) | 25(2) |
| 2 | 0.35 | 0.00(1) | 48.0(1) | 0.40(1) | 6(2) |
| *Doublets* | | | | | |
| 3 | 0.29 | 0.54(1) | | 0.40(1) | 9(2) |
| 4 | 0.26 | 1.08(1) | | 0.40(1) | 7(2) |
| singlet | 0.35 | | | | 53(2) |
| *Sextets* | | **20 K** | | | |
| 1 | 0.48 | 0.34(1) | 54.8(1) | 0.32(1) | 25(2) |
| 2 | 0.47 | -0.08(1) | 54.5(1) | 0.30(1) | 19(2) |
| 3 | 0.42 | 0.04(1) | 51.0(1) | 0.58(1) | 35(2) |
| 4 | 0.39 | -0.02(1) | 47.1(1) | 0.88(1) | 20(2) |

*The isomer shift (IS) is relative to $^{57}$Fe, QS (quadrupole splitting) = 1/2 $e^2qQ$, and Bhf to the magnetic hyperfine field at $^{57}$Fe nuclei. Γ is the linewidth.

**Table 4**

| | $(Bi_{0.75}Fe_{0.25})FeO_3$ | $(Bi_{0.85}Fe_{0.15})FeO_3$ | $BiFeO_3$* |
|---|---|---|---|
| ***Unit cell volume*** | | | |
| $M_0$ /$10^6$pm$^3$ | 372.4(9) | 371.9(8) | 372.39(1) / *373.10(5)* |
| $k_D$ /$10^{-12}$Pa$^{-1}$ | 9.5(24) | 8.91(2) | 8.71(1) / *8.30(1)* |
| $\theta_D$ /K | 357(89) | 392(81) | 361(30) / *328(42)* |
| ***Lattice parameter a*** | | | |
| $M_0$ /pm | 557.5(4) | 557.3(4) | 557.35(1) / *557.70(2)* |
| $k_D$ /$10^{-12}$Pa$^{-1}$ | 4.1(3) | 3.7(3) | 3.75(1) / *3.41(1)* |
| $\theta_D$ /K | 321(22) | 328(25) | 423(5) / *345(10)* |
| ***Lattice parameter c*** | | | |
| $M_0$ /pm | 1383.4(6) | 1382.1(2) | 1384.27(1) / *1384.95(5)* |
| $k_D$ /$10^{-12}$Pa$^{-1}$ | 12.7(6) | 12.7(2) | 13.82(1) / *13.27(2)* |
| $\theta_D$ /K | 268(12) | 269(5) | 306(7) / *234(23)* |

* data from Palewicz et al.[30,31] and Fischer et al.[3] (*Italic*)

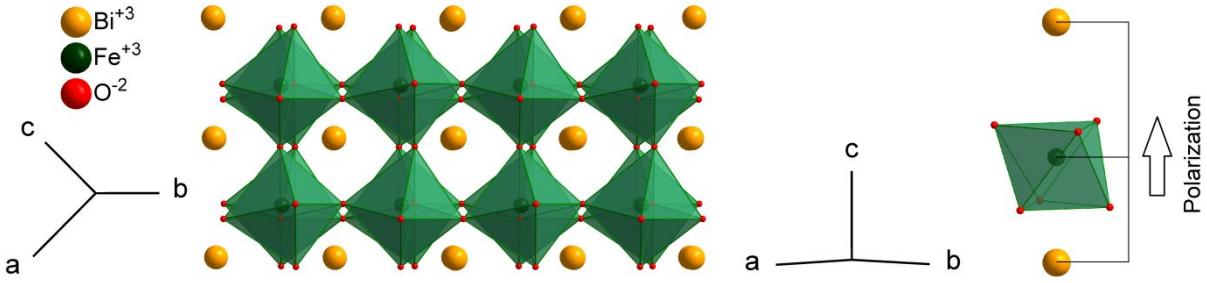


**Figure 1**

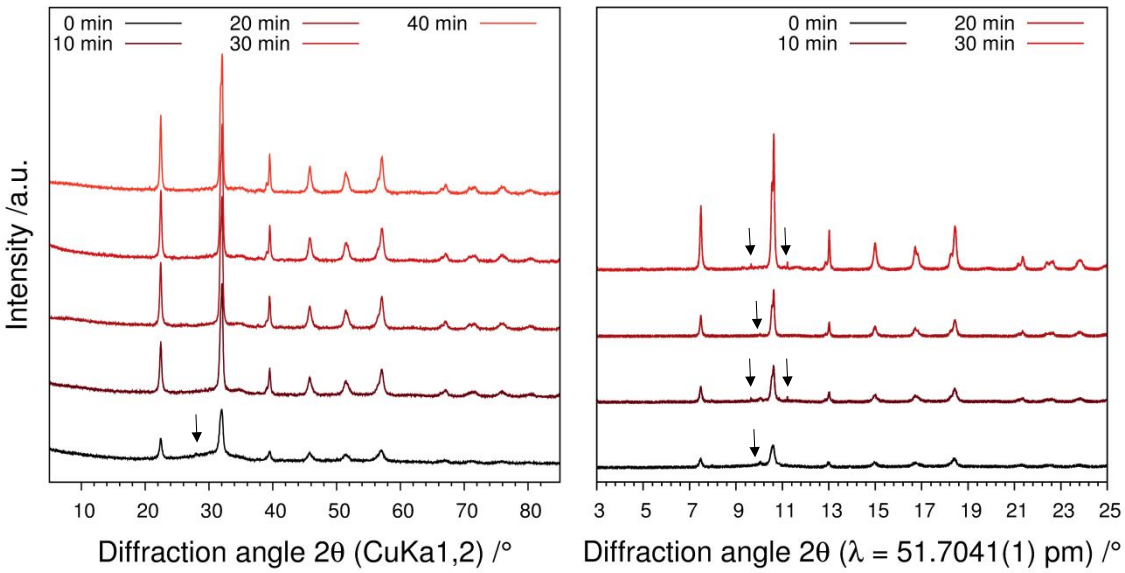


**Figure 2**

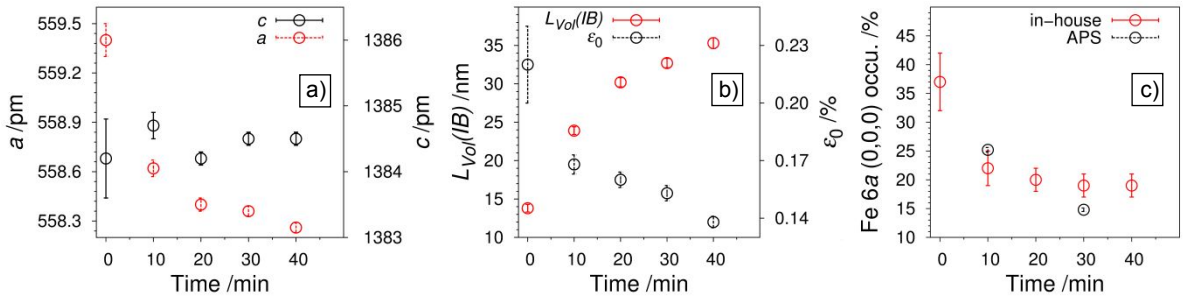


**Figure 3**

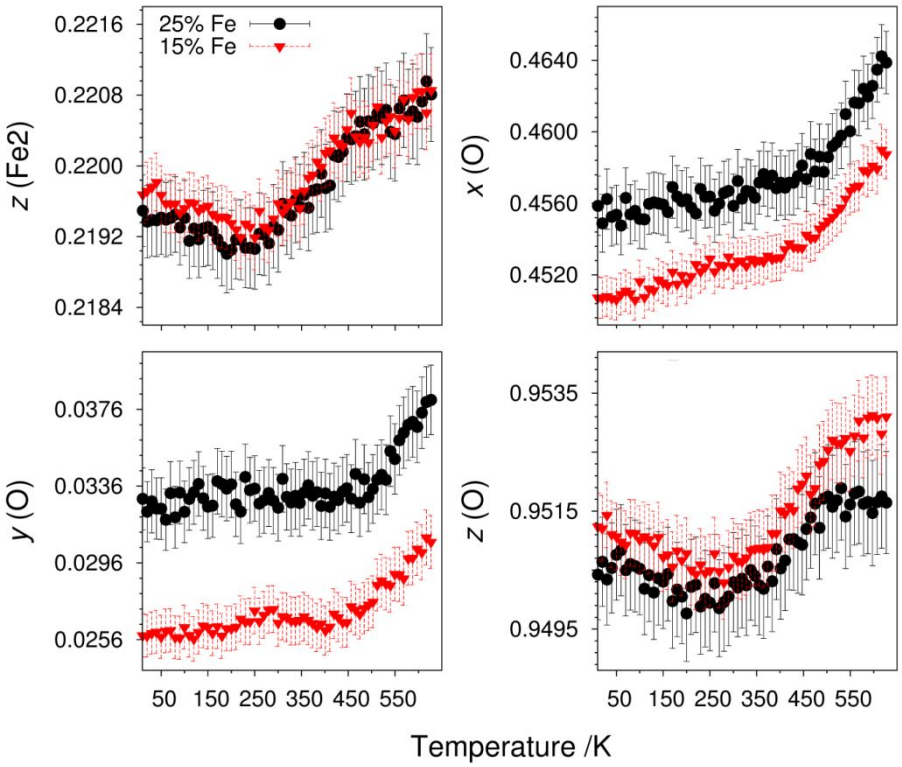


**Figure 4**

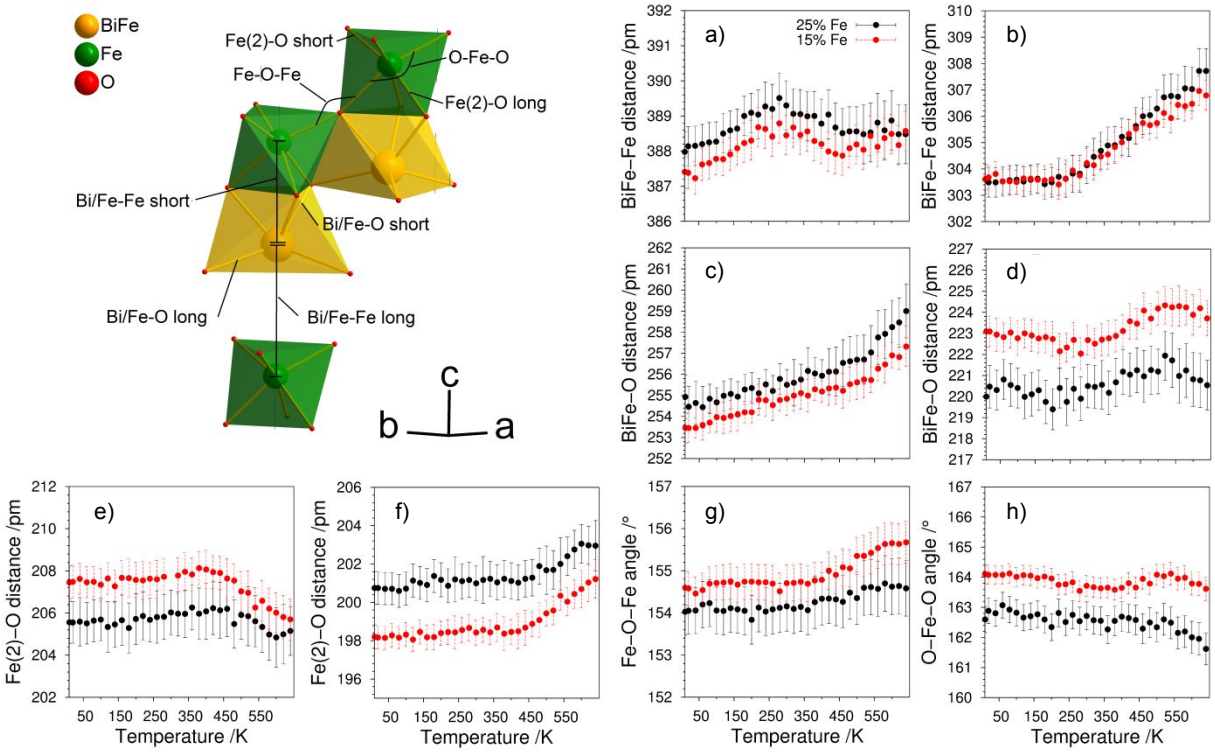


**Figure 5**

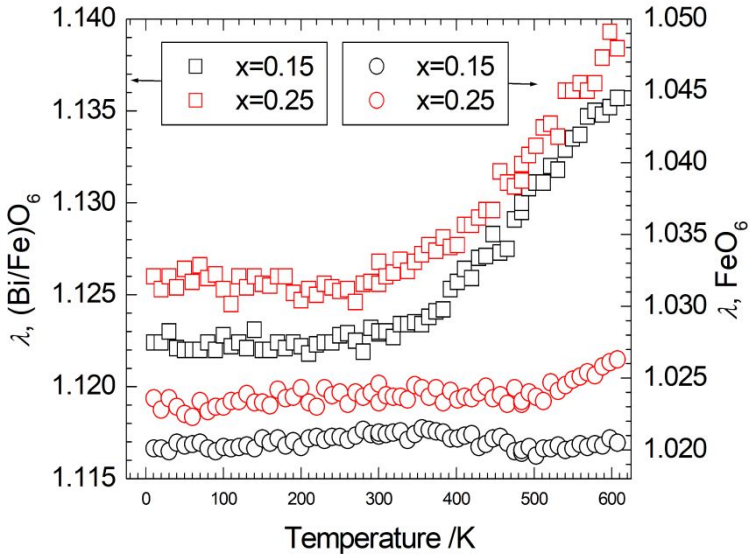


**Figure 6**

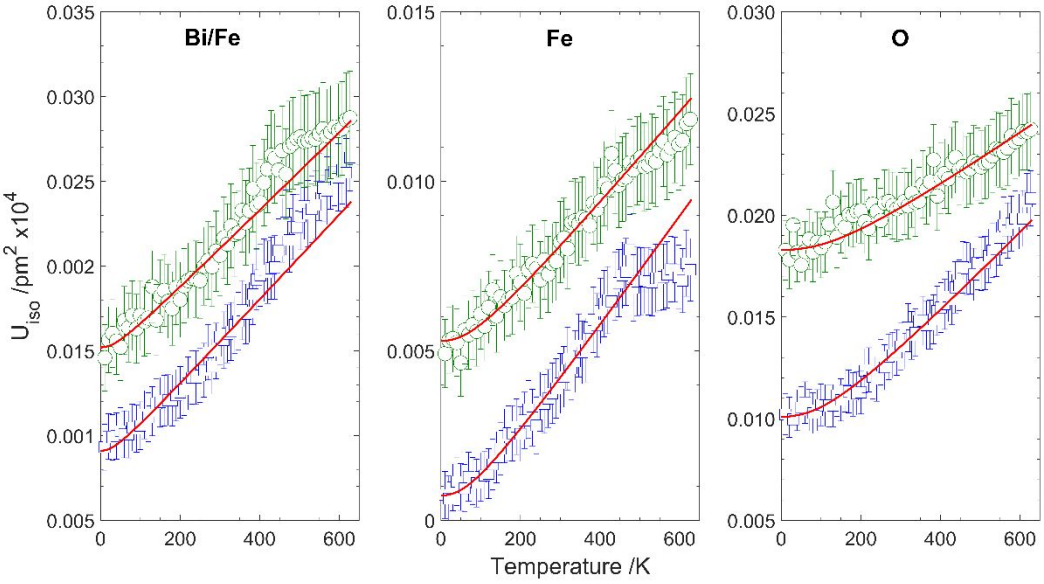


**Figure 7**

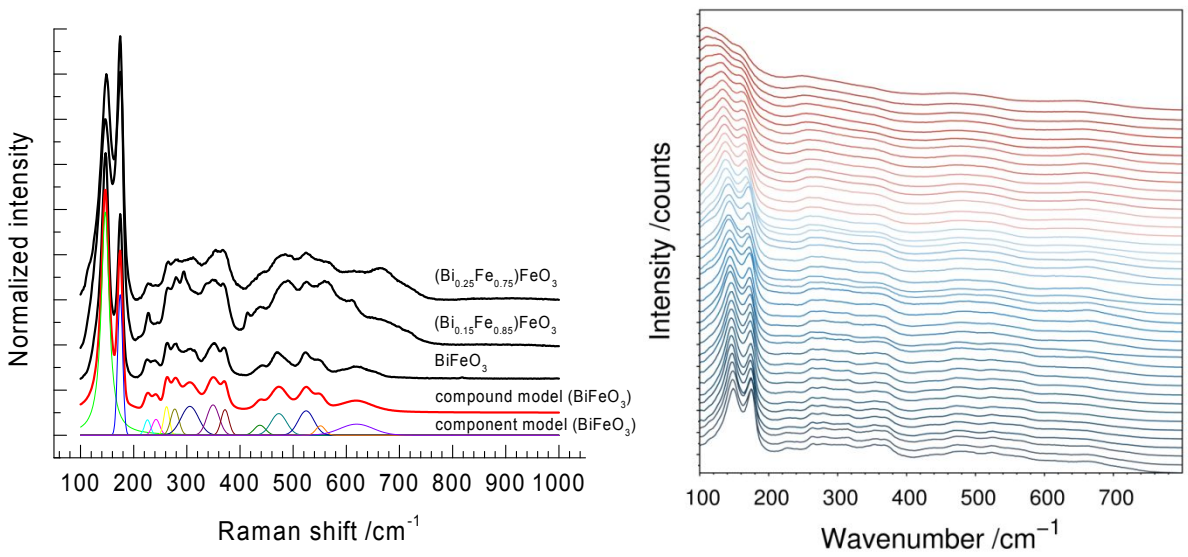
Normalized intensity
(Bi0.25Fe0.75)FeO3
(Bi0.15Fe0.85)FeO3
BiFeO3
compound model (BiFeO3)
component model (BiFeO3)
100 200 300 400 500 600 700 800 900 1000
Raman shift /cm-1
Intensity /counts
100 200 300 400 500 600 700
Wavenumber /cm−1

**Figure 8**

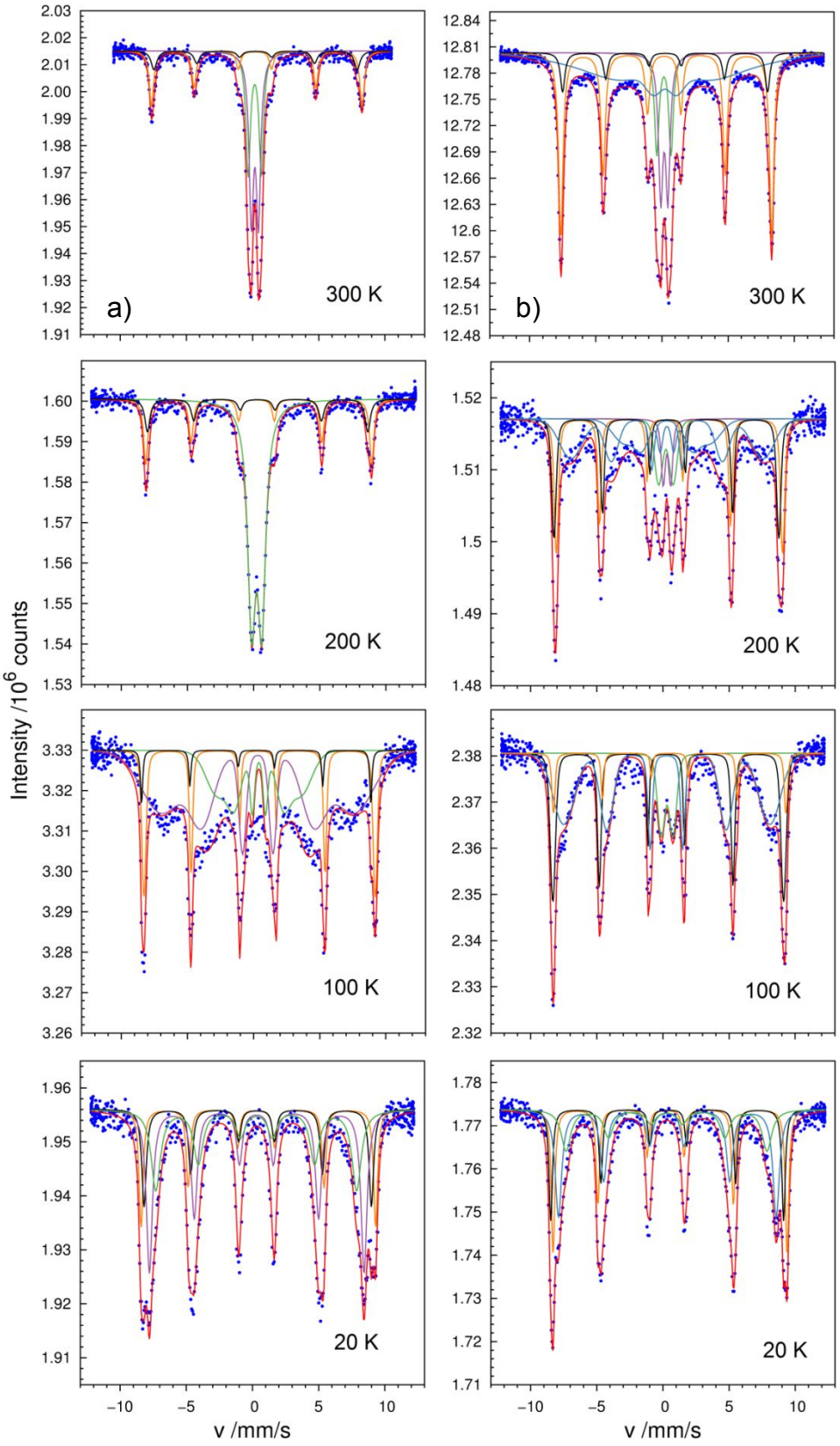
a)
300 K
b)
300 K
200 K
200 K
100 K
100 K
20 K
20 K
Intensity /10^6 counts
v /mm/s
v /mm/s

**Figure 9**

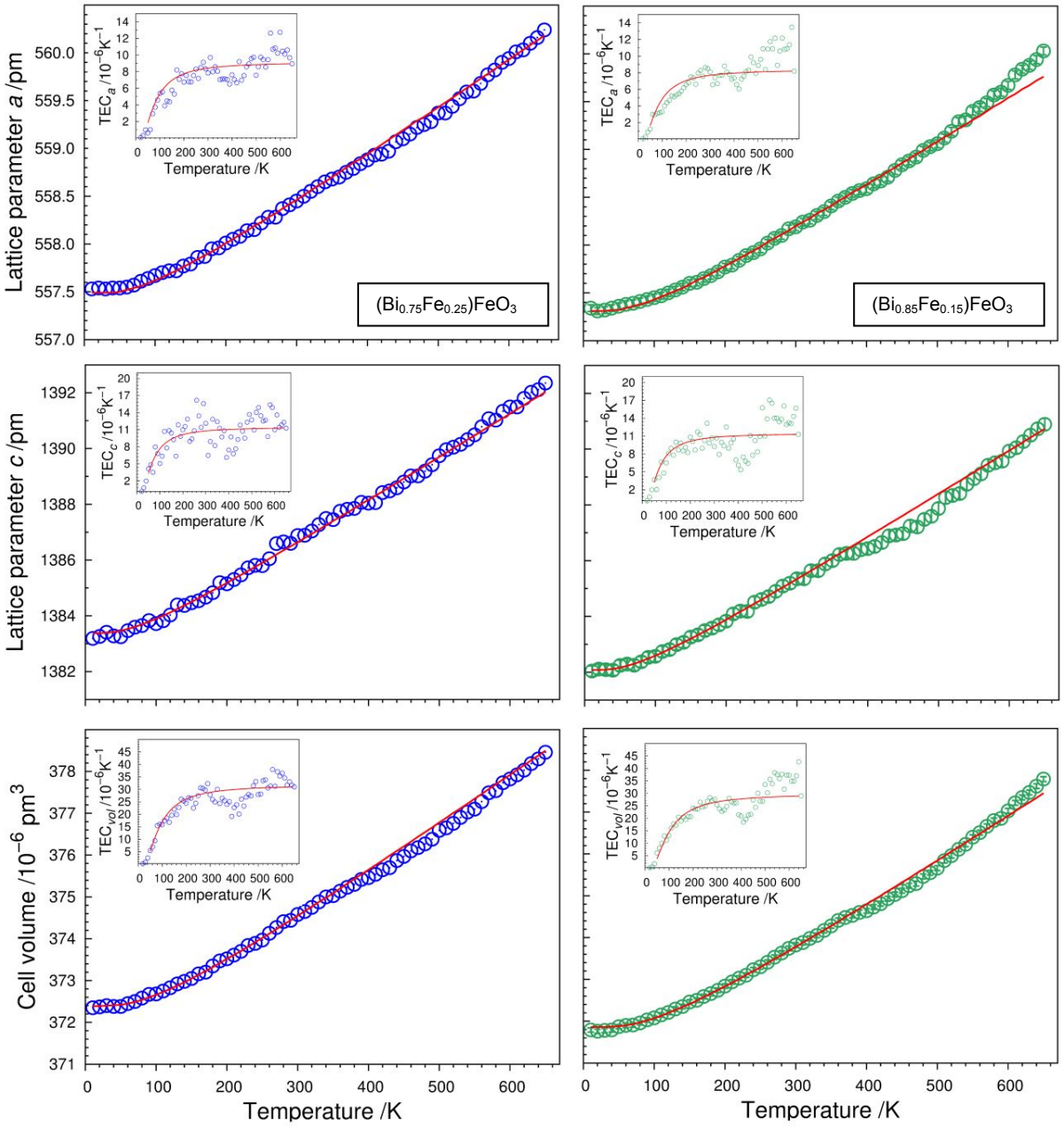
Lattice parameter a /pm
Lattice parameter c /pm
Cell volume /10−6 pm3
Temperature /K
TECa /10−6K−1
TECc /10−6K−1
TECvol /10−6K−1
(Bi0.75Fe0.25)FeO3
(Bi0.85Fe0.15)FeO3

**Figure 10**

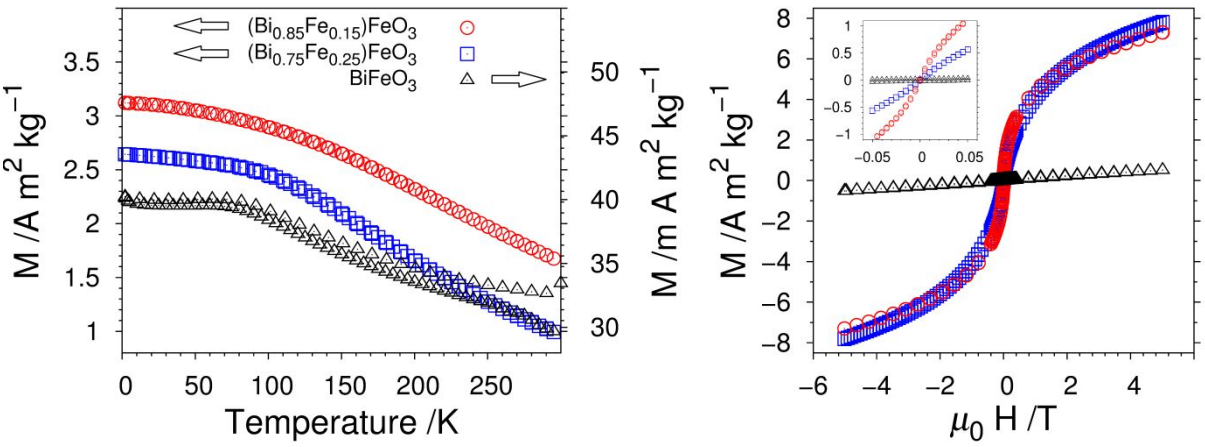
(Bi0.85Fe0.15)FeO3
(Bi0.75Fe0.25)FeO3
BiFeO3
M /A m2 kg−1
M /m A m2 kg−1
Temperature /K
μ0 H /T

**Figure 11**

## Table of contents graphic

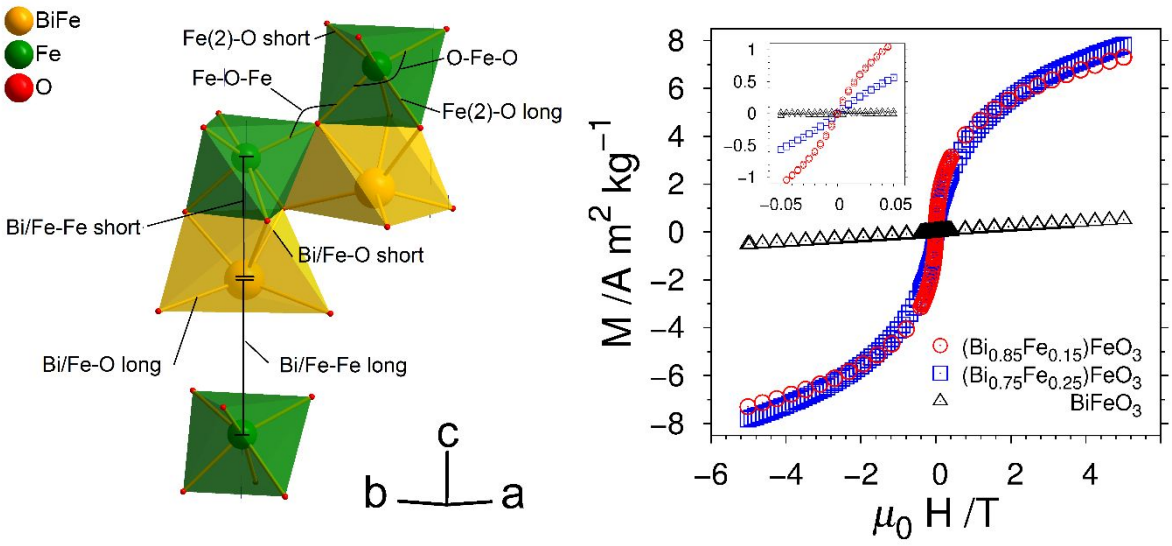


Coordination and connectivity in $(Bi_{1-x}Fe_x)FeO_3$. Magnetic hysteresis curves compare between the paramagnetic and the superparamagnetic behaviors.